

The diurnal evolution of ^{222}Rn and its progeny in the atmospheric boundary layer during the Wangara experiment

J.-F. Vinuesa¹, S. Basu², and S. Galmarini¹

¹European Commission - DG Joint Research Centre, Institute for Environment and Sustainability, 21020 Ispra, Italy

²Atmospheric Science Group – Department of Geosciences and Wind Science and Engineering Research Center, Texas Tech University, USA

Received: 10 May 2007 – Published in Atmos. Chem. Phys. Discuss.: 25 June 2007

Revised: 19 September 2007 – Accepted: 19 September 2007 – Published: 28 September 2007

Abstract. The diurnal atmospheric boundary layer evolution of the ^{222}Rn decaying family is studied using a state-of-the-art large-eddy simulation model. In particular, a diurnal cycle observed during the Wangara experiment is successfully simulated together with the effect of diurnal varying turbulent characteristics on radioactive compounds initially in a secular equilibrium. This study allows us to clearly analyze and identify the boundary layer processes driving the behaviour of ^{222}Rn and its progeny concentrations. An activity disequilibrium is observed in the nocturnal boundary layer due to the proximity of the radon source and the trapping of fresh ^{222}Rn close to the surface induced by the weak vertical transport. During the morning transition, the secular equilibrium is fast restored by the vigorous turbulent mixing. The evolution of ^{222}Rn and its progeny concentrations in the unsteady growing convective boundary layer depends on the strength of entrainment events.

1 Introduction

The diurnal structure of the atmospheric boundary layer (ABL) has an important impact on the dispersion of chemical compounds. The main characteristic of the ABL is its turbulent nature that drives scalar transport with a broad range of spatial and temporal scales. Turbulent eddy motions transport and mix primary and secondary pollutants throughout the ABL. Large-scale turbulent eddy motions (e.g., thermals and subsidence motions) characterize the daytime convective boundary layer while the nocturnal boundary has significantly smaller eddies.

In large-eddy simulation (LES), the largest eddies that are responsible for the turbulent transport of the scalars and mo-

mentum are explicitly solved whereas the smallest ones that are mainly dissipative are parameterized using a subgrid-scale (SGS) model. Since the seminal works by Deardorff (1970, 1972, 1974a,b, 1980), there have been numerous studies on LES of daytime buoyancy-driven boundary layers (Moeng and Wyngaard, 1984; Mason, 1989; Schumann, 1989; Sykes and Henn, 1989; Nieuwstadt et al., 1991; Khanna and Brasseur, 1997; Lewellen and Lewellen, 1998; Sullivan et al., 1998; Albertson et al., 1999), neutrally stratified ABL flows (Mason and Thomson, 1987; Andr n et al., 1994; Moeng and Sullivan, 1994; Lin et al., 1996; Kosovi c, 1997; Port -Agel et al., 2000; Esau, 2004; Bou-Zeid et al., 2005; Chow et al., 2005; Stoll and Port -Agel, 2006; Anderson et al., 2007), and stably stratified ABL flows (Mason and Derbyshire, 1990; Brown et al., 1994; Andr n, 1995; Saiki et al., 2000; Kosovi c and Curry, 2000; Basu and Port -Agel, 2006; Beare et al., 2006). LES has enabled researchers to study various boundary layer flows by generating unprecedented high-resolution four-dimensional atmospheric turbulence data.

The full diurnal ABL cycle consists of the three flow regimes mentioned above and two transition states after sunrise and after sunset. The main limitation in simulating the diurnal ABL cycle resides in the difficulty of resolving both the small scales that characterize the nocturnal boundary layer and the large ones of the day time case with the same sub-grid scale model. A successful LES depends on the ability to accurately simulate the dynamics that are not explicitly resolved. The increasing atmospheric stability conditions from day to nighttime flow enhances the difficulty to perform successful simulations.

A solution to the long standing issue of resolving the diurnal variation of the atmospheric boundary layer has recently been offered by the use of new generation scale-dependent dynamic subgrid-scale models (Kumar et al., 2006; Basu et al., 2007). Both models are tuning-free, i.e., they do not

Correspondence to: J.-F. Vinuesa
(jeff.vinuesa@jrc.it)

require any ad-hoc specification of SGS coefficients. Kumar et al. (2006) used a Lagrangian approach (Bou-Zeid et al., 2005) that calculates the Smagorinsky coefficient dynamically at every position in the flow and as the flow evolves in time following fluid particle trajectories. Basu et al. (2007) calculated both the Smagorinsky coefficient and the SGS Schmidt/Prandtl number using the locally-averaged scale-dependent dynamic (LASDD) SGS modeling approach (Basu and Porté-Agel, 2006; Basu et al., 2006; Anderson et al., 2007). In addition, Basu et al. (2007) have demonstrated that the tuning-free LASDD SGS model based LES has the ability to capture the fundamental characteristics of observed atmospheric boundary layers even for very coarse resolutions.

Atmospheric dispersion of radon and its progeny has been of considerable interest for a number of years. ^{222}Rn is an unstable noble gas isotope of ^{226}Ra with a half-life ($\tau_{1/2}$) of 3.8 days. Ground-based measurements and vertical distributions have been extensively studied to characterize the turbulent properties of the ABL, to perform regional and global circulation model benchmarking and to estimate regional surface fluxes of air pollutant and in particular climatically sensitive compounds. For instance, from one year measurements Galmarini (2006) once more demonstrated the ^{222}Rn ability of being an excellent tracer for boundary layer studies, Li and Chang (1996) used ^{222}Rn simulations to evaluate the modeled transport processes in a 3-D global chemical transport model, Dentener et al. (1999) compared their model results with measurements to investigate the resolution sensitivity of their code, and Genthon and Armengaud (1995) or Jacob et al. (1997), among others, performed global atmospheric models evaluation and comparison using ^{222}Rn .

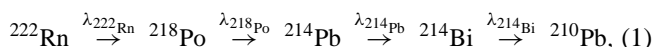
Despite many experimental studies in the literature, there have been very few studies that have reported measurements of the vertical variation of radon and its daughters through the whole ABL under a variety of conditions. This has been mainly attributed to the slow development of detection technology of suitable accuracy that can practically be mounted on an aircraft. In the absence of such datasets, LES is an option and in a recent study, Vinuesa and Galmarini (2007) used for the first time LES to characterize the turbulent transport of the ^{222}Rn and its progeny in academic ABLs. They simulated a steady-state convective ABL and ABL under unsteady conditions, e.g., representing the morning transition. They showed that the turbulent properties of atmospheric convective boundary layers are of importance to study the dispersion and the transport of the ^{222}Rn family. In this present study, we broaden the recent work of Vinuesa and Galmarini (2007) by extending the study of the control exerted by turbulence on ^{222}Rn and its progeny atmospheric dispersion to the full range of stabilities characterizing atmospheric boundary layers. Not only do we corroborate their findings for the unsteady convective boundary layer but we generalize and complete the study by simulating a realistic diurnal cycle consisting of the three stability regimes i.e. stable, neutral and un-

stable. In addition, by imposing secular equilibrium as initial condition, the issue of its possible disruption due to atmospheric stability can be addressed.

The paper is structured as follows. In Sect. 2, we describe the radioactive decay chain of ^{222}Rn . Simulation details of the observed case study are discussed in Sect. 3. In Sect. 4, general results on the diurnal dispersion of ^{222}Rn and its progeny are presented. These results are detailed in the three following sections by focusing on the dispersion during the night, the daytime turbulent dispersion and the evolution of the mixed-layer quantities. Section 8 is devoted to the disruption of the secular equilibrium due to the atmospheric stability and an analysis of the disequilibrium activity ratios of ^{222}Rn and its short-lived daughters is provided. Finally, concluding remarks are drawn in Sect. 9.

2 ^{222}Rn decaying chain and turbulent dispersion

We consider the radioactive decay chain of ^{222}Rn that reads:



where $\lambda_{222}\text{Rn}$, $\lambda_{218}\text{Po}$, $\lambda_{214}\text{Pb}$ and $\lambda_{214}\text{Bi}$ are the decay frequencies (related to the half-life by $\tau_{1/2} = \ln 2 / \lambda$) equal to $2.11 \times 10^{-6} \text{ s}^{-1}$ ($\tau_{1/2} = 3.8$ days), $3.80 \times 10^{-3} \text{ s}^{-1}$ ($\tau_{1/2} = 3.04$ min), $4.31 \times 10^{-4} \text{ s}^{-1}$ ($\tau_{1/2} = 26.8$ min), and $5.08 \times 10^{-4} \text{ s}^{-1}$ ($\tau_{1/2} = 19.9$ min), respectively. Note that we consider a direct transformation of ^{214}Bi into ^{210}Pb since the half-life of ^{214}Po (daughter of ^{214}Bi) is very short (164 μs). Also we consider ^{210}Pb , that has a half-life of 22.3 years, as an inert scalar with respect to the temporal scales considered here. To increase readability, ^{222}Rn and its progeny activity concentrations (measured in Bq, or atomic disintegrations per second) will be also referred to as S_i where i is the rank of the daughter in the decay chain (e.g., 0 stands for ^{222}Rn and 4 for ^{210}Pb). In the following n_i stand for the concentration in the number of atoms of the daughter i .

In large-eddy simulation, the filtered conservation equation for a radioactive scalar involved in a chain of reactions is

$$\frac{\partial \tilde{n}_i}{\partial t} + \tilde{u}_j \frac{\partial \tilde{n}_i}{\partial x_j} = - \frac{\partial Q_{i,j}}{\partial x_j} + \tilde{R}_i \quad (2)$$

where \tilde{n}_i is the spatially filtered scalar concentration n_i , \tilde{R}_i is its radioactive source/sink term and $Q_{i,j}$ is its subgrid-scale (SGS) flux defined as:

$$Q_{i,j} = \tilde{u}_j \tilde{n}_i - \tilde{u}_j \tilde{n}_i, \quad (3)$$

For the chain (1), the \tilde{R}_i read:

$$\tilde{R}_0 = -\lambda_0 \tilde{n}_0, \quad (4)$$

$$\tilde{R}_1 = \lambda_0 \tilde{n}_0 - \lambda_1 \tilde{n}_1, \quad (5)$$

$$\tilde{R}_2 = \lambda_1 \tilde{n}_1 - \lambda_2 \tilde{n}_2, \quad (6)$$

$$\tilde{R}_3 = \lambda_2 \tilde{n}_2 - \lambda_3 \tilde{n}_3, \quad (7)$$

$$\tilde{R}_4 = \lambda_3 \tilde{n}_3. \quad (8)$$

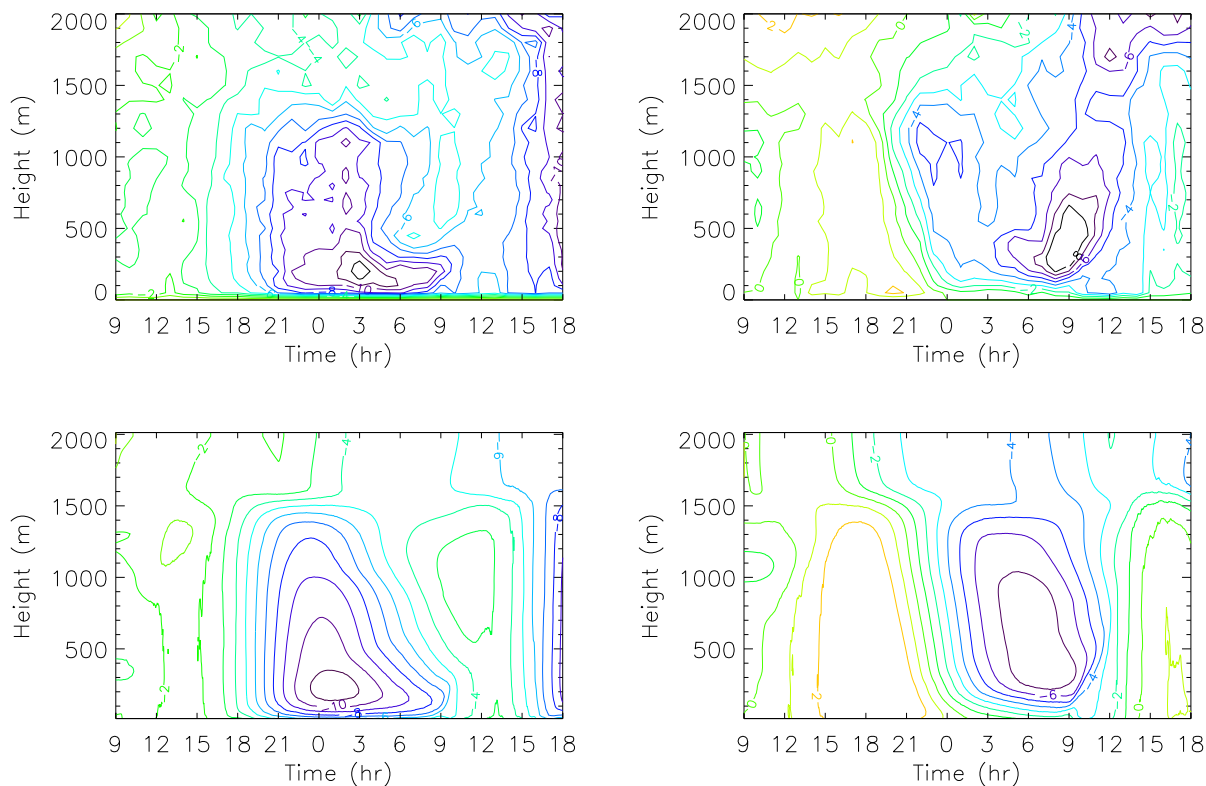


Fig. 1. Time-height plots of the observed (top) and modeled (bottom) mean longitudinal (left) and lateral (right) velocity components.

As one can see, the process is unidirectional with the concentration of ^{222}Rn initial concentration flowing from daughter to daughter. In such condition, the expected effect of turbulence will relate to the mixing of the different species. One could expect that species produced faster than others may accumulate in specific regions of the ABL at different rates, due to turbulent transport and mixing processes. The timescale of the turbulent transport and how it relates to the timescale of the radioactive decay is one of the governing parameters of the process.

The deviation from the secular equilibrium is often used as an indicator of the residence time in the atmosphere or as an indicator of the atmospheric stability. The secular equilibrium is the condition according to which the ratio of the activities of the nuclide participating to the decay chain is equal to 1, namely:

$$\frac{\lambda_{i+1} \widetilde{n}_{i+1}}{\lambda_i \widetilde{n}_i} = 1 \quad (9)$$

so that $\widetilde{R}_{i+1} = 0$ for $i=0,1,2$. This corresponds to a balance between production and destruction of the nuclide. One of the foci of this study is to determine whether an initially imposed secular equilibrium is disrupted during the full daily evolution of the ABL and given a constant in-flux of ^{222}Rn at the

surface as due to the simultaneous occurrence of mixing and radioactive decay.

3 Description of the simulation

In this work, the simulation is performed with a modified version of 3-dimensional LES code described by Albertson et al. (1999); Porté-Agel et al. (2000); Porté-Agel (2004) in which a chemical solver has been recently introduced (Vinuesa and Porté-Agel, 2005). We use the newly proposed “locally-averaged scale-dependent dynamic” (LASDD) SGS modeling approach (Basu and Porté-Agel, 2006; Basu et al., 2006; Anderson et al., 2007) for simulations of an diurnal cycle observed during Wangara experiment. The LASDD SGS model is completely tuning-free in contrast to most of the conventional eddy-viscosity and eddy-diffusivity SGS models. In other words, the LASDD SGS model does not require any ad-hoc specification of SGS coefficients, since they are computed dynamically based on the local dynamics of the resolved velocity and temperature fields in a self-consistent manner.

The Wangara experiment was conducted during July and August 1967 at Hay in Australia (Clarke et al., 1971; Hess et al., 1981). Basu et al. (2007) presented the first LES study

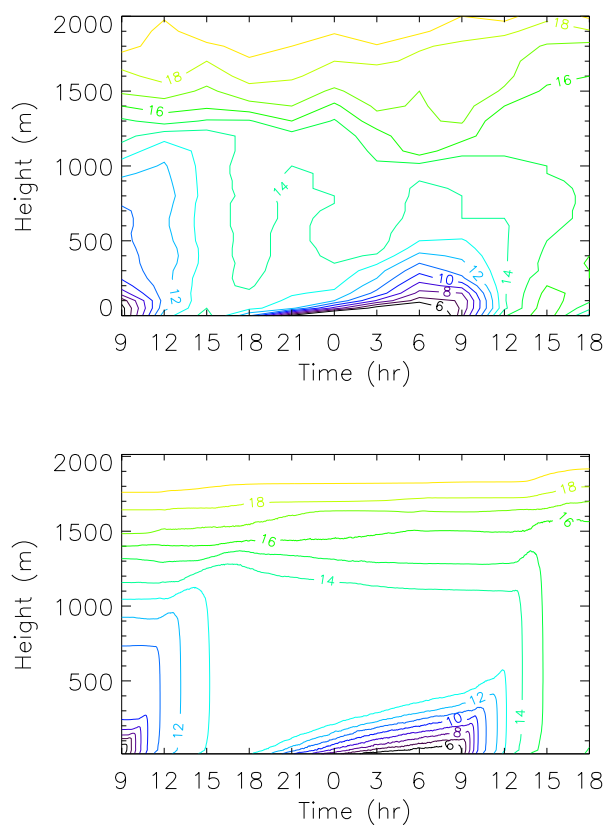


Fig. 2. Time-height plot of the observed (top) and modeled (bottom) mean potential temperature ($^{\circ}\text{C}$).

of a diurnally varying ABL observed during the Wangara case study. Their simulation were performed for a full diurnal cycle, from 09:00 LST, day 33 (16 August 1967) to 09:00 LST, day 34 (17 August 1967). In the present study, we are also interested in the interaction between the ABL and the reservoir layer above it, we extend the simulation up to 18:00 LST of day 34. Since the initialization of the simulation, the surface and large-scale forcing are fully detailed in Basu et al. (2007), we only give here a brief summary.

The LES model is initialized with 09:00 LST sounding of day 33. The lower boundary condition is based on the Monin-Obukhov similarity theory with a surface roughness length $z_0=0.01$ m. Following Yamada and Mellor (1975), the screen temperature at 1.2 m is used for sensible heat flux estimation and vertical profiles of geostrophic wind components (U_g , V_g) at any instant are calculated by fitting parabolic profiles to the observed surface geostrophic wind and thermal wind values. Finally, these values are linearly interpolated between the observation times (see Yamada and Mellor, 1975, for further details). The Coriolis parameter is set to $f_c=-0.826\times 10^{-4}$ s^{-1} corresponding to latitude $34^{\circ}30'$ S. Following previous studies (e.g., Jacobi and Andre, 1963; Beck and Gogolak, 1979), the exhalation rate of radon is set

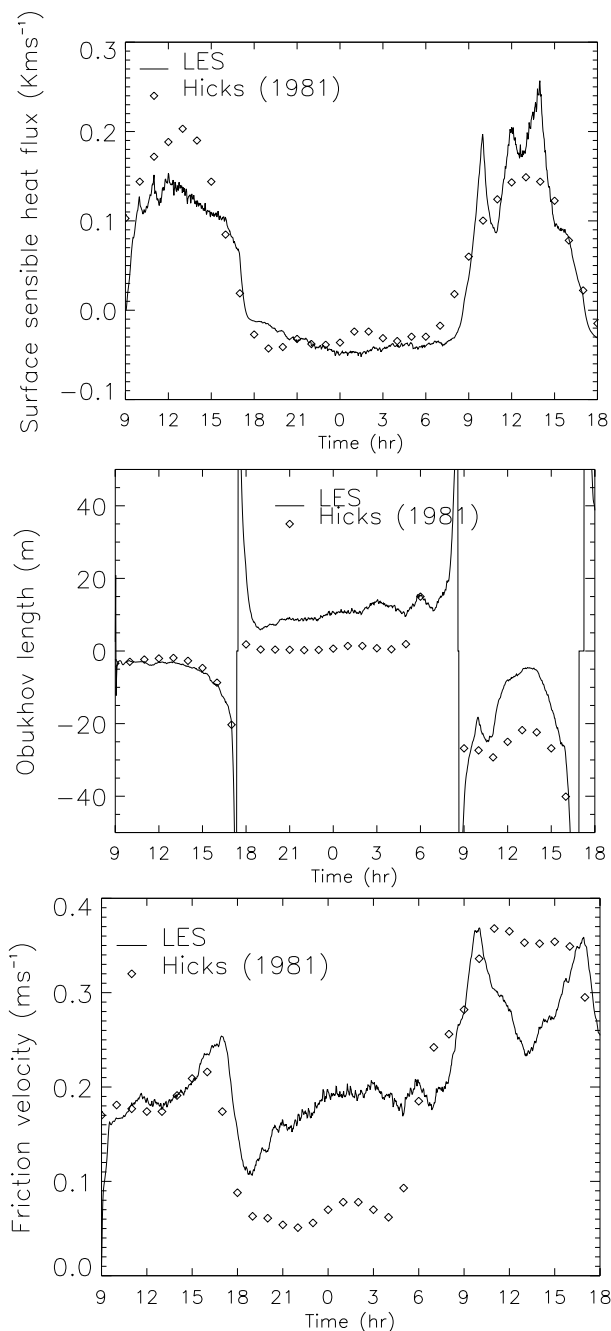


Fig. 3. Evolution of the sensible surface heat flux, the friction velocity and the Obukhov length. The diamonds are from the analyses of the Wangara observations by Hicks (1981).

at typical value of 1.0 $\text{atom cm}^{-2} \text{s}^{-1}$. The initial radon concentration is set at 10.0 Bq m^{-3} in the ABL as this is the value generally assumed to be a global average measured close to land surface (UNSCEAR, 2000). Above the ABL, we assume a zero background concentration. A secular equilibrium between radon and its progeny is imposed as initial condition.

The selected domain size is $5000\text{ m} \times 5000\text{ m} \times 2000\text{ m}$. In Basu et al. (2007), this domain was divided into: $160 \times 160 \times 160$ grid-points. However, Basu and Porté-Agel (2006) found that the LASDD model simulated statistics are quite insensitive to grid resolution. This was confirmed by Basu et al. (2007) that showed that even with a coarse resolution of $80 \times 80 \times 80$ grid points, the LASDD SGS model is able to capture the essential characteristics of the observed nighttime boundary layer (e.g., the magnitude, timing and location of the low-level jet wind maxima). Thus, we choose this latter resolution for the present study since the CPU demand and space requirement are enhanced by the addition of the radioactive decaying chain in the simulation. This leads to a grid resolution of $62.5\text{ m} \times 62.5\text{ m} \times 25.0\text{ m}$. Periodic lateral boundary conditions are assumed and the time step is set to 1 s.

The results relative to the wind and the potential temperature are briefly summarized in the following, see Basu et al. (2007) for a complete analysis.

Figure 1 shows the observed and simulated longitudinal and lateral components of velocity. During daytime, as a result of turbulent mixing, the wind profiles were observed to be nearly constant in the mixed layer. During night 33–34, a low-level jet (LLJ) developed due to inertial oscillation. Initially, the magnitude of the LLJ wind maxima increased with time (till approximately 03:00 LST) and then decreased. The observed LLJ height was approximately 200 m. From this figure, it is clear that our LES model has successfully captured the development, magnitude and location of the observed LLJ.

The evolution of simulated mean temperatures is compared with observations in Fig. 2. A thin, very unstable surface layer, and mixed layer topped by a stable inversion layer are discernible during the two daytimes. At nighttime, strong surface based inversion develops as would be expected. These features are qualitatively well reproduced by the LES model.

Figure 3 shows the evolution of the sensible surface heat flux, the friction velocity and the Obukhov length together with the analyses of the Wangara observations by Hicks (1981). During daytime, the simulated surface heat flux is smaller than observed however the nighttime one is well captured by the LES model. The simulated surface friction velocity evolution agrees well with observations during daytime. The LES model also captures the sudden decrease (increase) in friction velocity during evening (morning) transition. However, overestimation is clearly noticeable at night. As a result of overestimation of the surface friction velocity, the Obukhov length (L) is also overestimated during night.

4 Diurnal evolution of ^{222}Rn and its progeny concentrations during the Wangara experiment

In the following sections, we focus our analysis on the 24-h diurnal cycle starting at 18:00 LST on Day 33. The part of the simulation chosen to perform our analysis corresponds to a situation with realistic concentration profiles of ^{222}Rn and its progeny in the reservoir layer. Thus the beginning of the simulation, i.e. from 09:00 LST to 18:00 LST of day 33 allowed us to reproduce a realistic distribution of the nuclide in the atmosphere and then reduce the inherent forcing due to an imposed uniform initial distributions. In other terms, this period can be considered as a spin-up period of the simulation that allows a realistic spatial distribution consistent with boundary-layer mixing processes and secular equilibrium. In this section, the overall diurnal cycle is analyzed whereas the next two will focus on the specific processes responsible for the dispersion during the night and the day.

Figure 4 shows the time evolution of the concentration of the mother ^{222}Rn (S_0) and its progeny. Around sunset, vertical motions are suppressed due to the cooling at the surface. This cooling results in a stable temperature stratification and in the formation of a thin boundary layer isolating the surface from the residual layer above where turbulence decays. The nocturnal BL is characterized by very high radon concentrations and significant vertical concentration gradients. Over the night, S_0 is emitted constantly and, due to the stability of the NBL, it is accumulating close to the surface. S_0 and its short-lived daughters undergo the unidirectional chain of reactions with the radon concentration flowing into the daughter's. As a result, S_0 progeny also accumulates close to the surface.

At sunrise, the solar heating causes thermal plumes to rise. These plumes extend up to the top of the atmospheric boundary layer where a thermodynamic equilibrium is reached. Air from the free atmosphere penetrates down, replacing rising air parcels. Narrow vigorous thermals surrounded by relatively large subsidence motions generate turbulent mixing leading to a so-called mixed layer where, for instance, potential temperature is nearly constant with height. During the morning transition and the development of the unstable boundary layer, we find results similar to Vinuesa and Galmarini (2007). The concentration of all radio nuclei reduces abruptly in spite of the fresh emission of S_0 . These concentrations are driven by the production through the decaying chain, the dilution due to boundary layer deepening and the entrainment of lower concentration air masses from the reservoir layers. Under unstable conditions, dilution is driving the concentration behavior.

The reservoir layer is decoupled from the surface during nighttime due to the stable stratification of the nocturnal boundary layer and during daytime due to the capping inversion at the top of the convective boundary layer. No fresh emissions of S_0 can reach the reservoir layer and the radionuclide concentrations are decreasing with time.

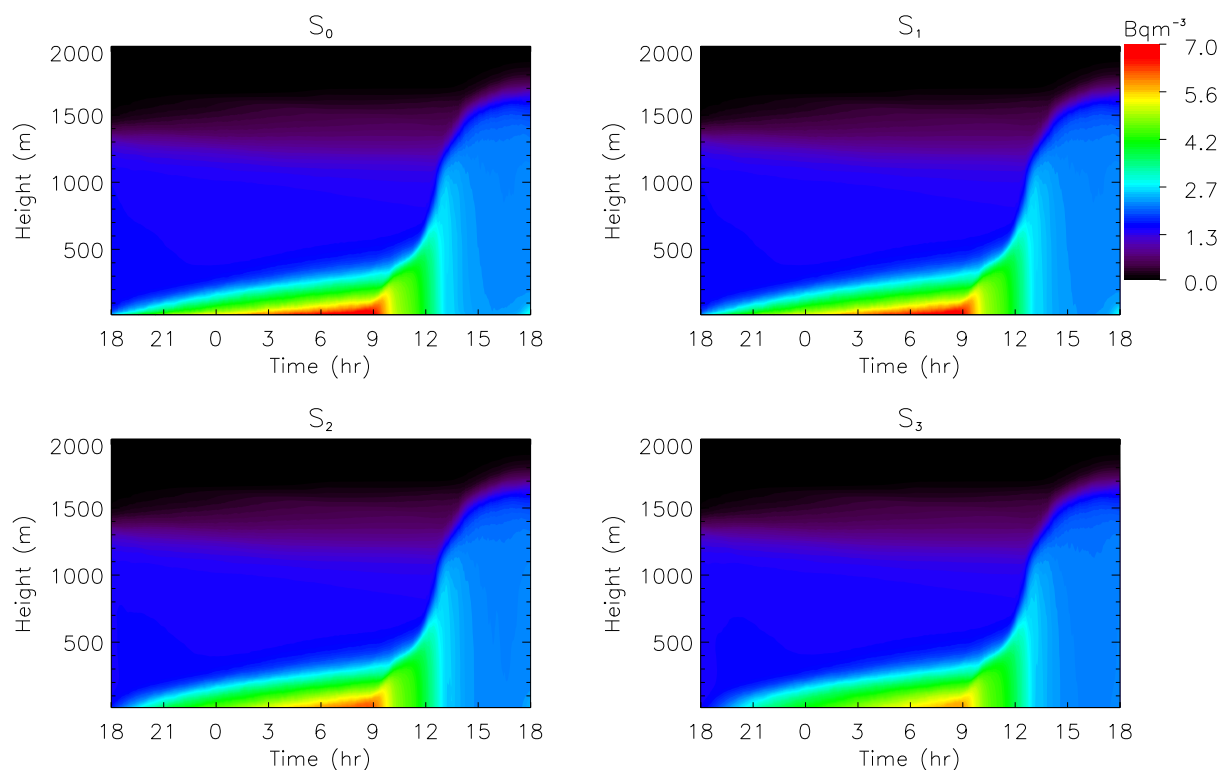


Fig. 4. Time-height plot of S_0 and its progeny.

The time evolution of the concentrations is the result of the combined effect of the divergence of the fluxes and the radioactive decay contribution. In order to understand which process is responsible for the ^{222}Rn and its short-lived daughters activity behavior, we will focus on the fluxes and the radioactive decay contributions in the next two sections. For the daytime period, one will notice that we found similar results as Vinuesa and Galmarini (2007) in their academic unsteady CBL simulation. Actually the present findings extend and corroborate their results to a full diurnal cycle, a realistic planetary boundary layer and a radon decaying family in or close to the secular equilibrium.

5 Dispersion during the night

In this section, we focus on the nighttime dispersion of radon and its progeny and we analyze the results for the stable nocturnal period from 18:00 LST on day 33 to 08:00 LST on day 34. The evolution of the sensible surface heat flux dynamically calculated from prescribed screen temperature at 1.2 m and temperature at first LES model level is shown in Fig. 3. As a result, the cooling at the surface occurs from 17:30 LST to 08:30 LST. The nocturnal boundary layer depth is ranging from 100 to 500 m and we will focus on this part of the atmosphere.

The low level stratification of the nocturnal boundary layer induces the accumulation of freshly emitted S_0 close to the surface (Fig. 7). In this area, the proportion of freshly emitted radon is higher than above. This layer can be considered as a “fresh radon layer” and since radon is slowly decaying, the proportion of freshly created daughters to radon is smaller than in upper regions. As a result, the presence of the “fresh radon layer” induces a rapid departure from secular equilibrium (see also Fig. 15, discussed in Sect. 8). The disequilibrium prevails during the night since fresh radon is constantly injected at the surface. As a result, S_0 concentrations show an almost linear increase whereas the build up of the daughters’ concentrations is slower and delayed, as seen in Fig. 7. The weak vertical mixing is responsible for the accumulation of radon and its progeny close to the surface.

The important temporal variability of the fluxes suggests that vertical transport events are very localized in space and time (Fig. 8). One can note that while the maximum vertical fluxes of radon are located close to the surface, the location of the maximum flux for its daughters moves upwards with increasing rank. These flux maxima correspond to the altitudes where the vertical concentration gradients are strongest. In contrast, the radioactive decay contributions to the short-lived daughter concentrations show maxima very close to the surface, and Fig. 9 reveals strong vertical gradients away from the surface for all the daughters. These

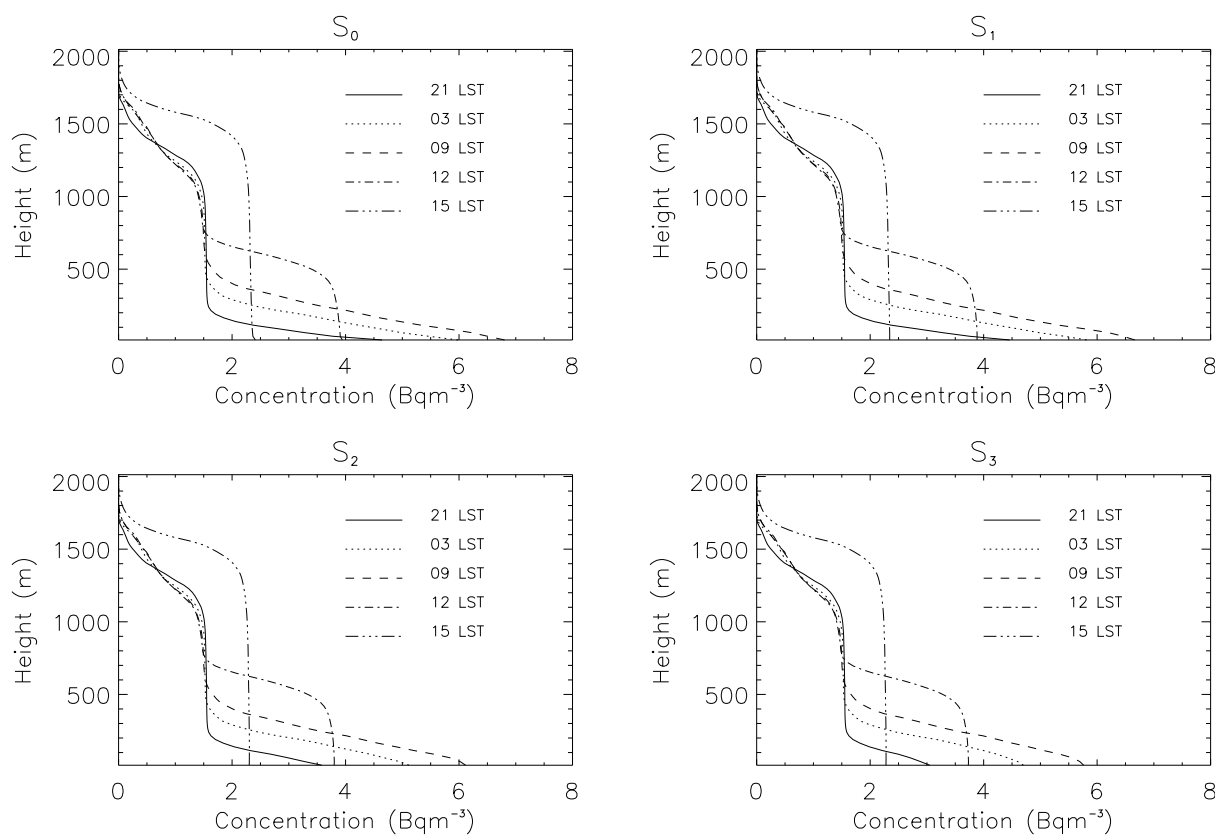


Fig. 5. Vertical profiles of S_0 and its progeny.

gradients are related to the concentration imbalance between the members of radon decaying family. Since ^{218}Po (S_1) is the first daughter of the family, its production by the decay of S_0 is more important where the S_0 concentrations are higher, i.e. close to the surface. Its radioactive decay proceeds at a faster rate than the mixing. Since mixing is very weak in the NBL, freshly created ^{218}Po is decaying before being transported. As a result, its radioactive contribution is mostly acting close to the surface. The same process occurs for R_2 and R_3 , although, due to the slower decaying rates of (S_2) and (S_3), the vertical gradients are not as strong as for R_1 .

6 Daytime turbulent dispersion

Figure 10 shows the daytime evolution of the concentration of ^{222}Rn (S_0) and the short-lived daughters S_1 , S_2 and S_3 . No fresh emissions of S_0 reach the reservoir layer resulting from the previous day CBL and from the nocturnal BL since they are decoupled from the surface. Radon and its progeny concentrations decrease with time in the reservoir layer as result of the decaying process. In the CBL, similar concentration behaviors can be observed for S_0 and the daughters: as the boundary layer deepens with time, the concentrations

decrease despite of fresh emission of radon at the surface and the production of the daughters through the decay chain. As mentioned previously, this behavior is the result of an imbalance between production by surface emissions and the decaying chain on one hand, and dilution by boundary layer deepening and ventilation on the other. In order to understand the processes dominating the collapse of the ^{222}Rn and its short-lived daughters concentration during the morning transition of the convective boundary layer, we focus in the following on the vertical profiles of the fluxes (Fig. 11) and the radioactive decay contributions (Fig. 12).

The growth of the boundary layer is inducing ventilation at the top of the CBL. While the boundary layer is deepening, air masses with smaller concentrations are entrained from above. Turbulence transport is locally balancing the gradient of concentration induced by the entrainment of cleaner air by transporting radionuclides from within the CBL towards its upper boundary (Fig. 11). This upward flux is more vigorous when the ventilation process is enhanced by the increase of the boundary layer growth rate. As a result we found important detrainment fluxes, i.e. positive flux values at the entrainment interface, that were even larger than the emission flux for S_0 at the surface. Actually, two detrainment flux maxima can be noted when looking closely to the

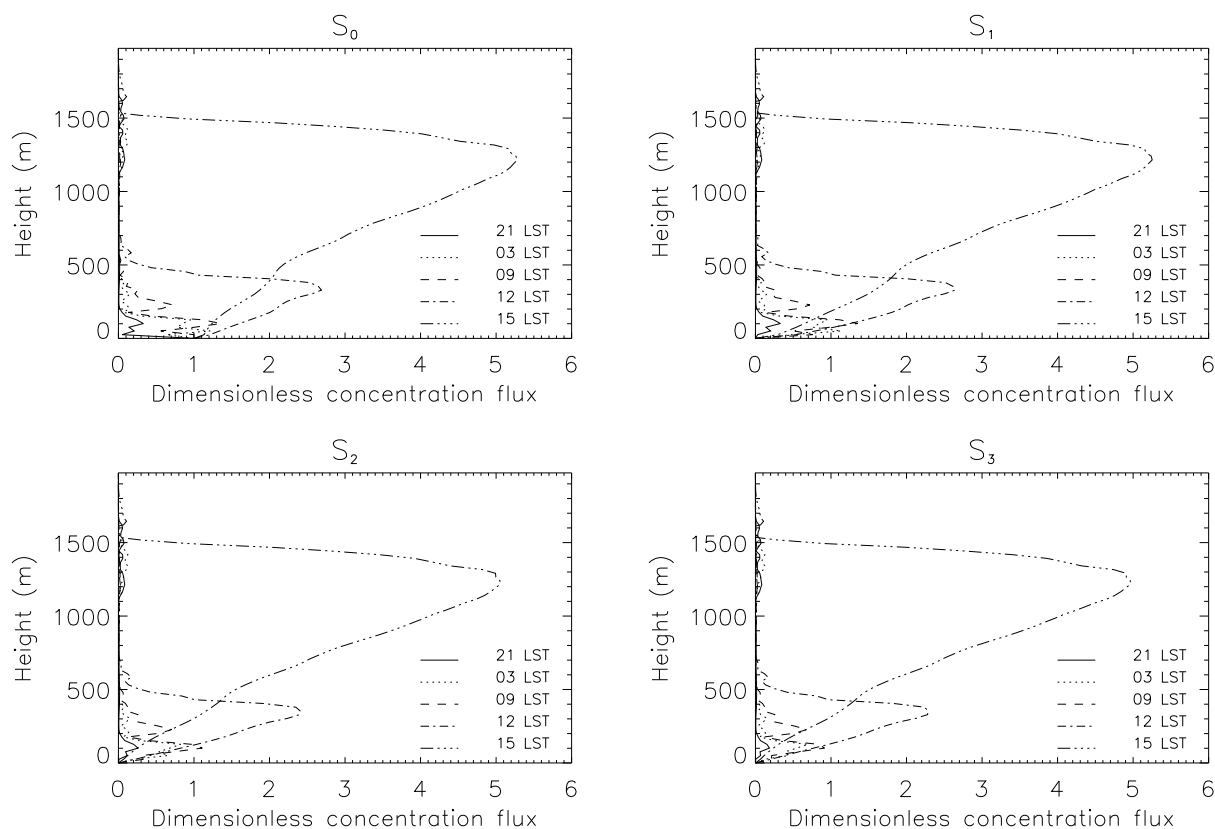


Fig. 6. Vertical profiles of the fluxes of S_0 and its progeny. The fluxes are made dimensionless by using the exhalation rate of radon.

figure: one at 10:00 LST and the one at around 12:30 LST. These maxima occur when the growth of the boundary layer depth, and therefore also the entrainment velocity w_e , shows a maximum (see Fig. 13, discussed in Sect. 7). This confirms that the high flux values are due to the entrainment of low concentration air masses from above the CBL.

The radioactive decay term (Fig. 12) acts as a sink for S_0 and as a source for its progeny. All contributions show a maximum close to the surface, but with different vertical gradients: the gradient of R_1 is extreme compared to those of R_2 and R_3 , which show almost well-mixed profiles in the lower-CBL and a maximum contribution at the bottom of the entrainment layer. This behavior was already mentioned by Vinuesa and Galmarini (2007) that attributed it to the inability of turbulence to mix efficiently radon short-lived daughters that have a decaying temporal scale comparable to the turnover time of the CBL. Our findings confirm their analysis for a more realistic simulation.

7 Focusing on the mixed-layer characteristics

Figure 13 shows the evolution of the convective boundary layer growth focusing on the boundary layer depth z_i defined as the height where the minimum sensible heat flux is found,

the entrainment velocity w_e that is the speed of the boundary layer growth, i.e. $\frac{dz_i}{dt}$ and the ratio of entrainment to the surface flux of potential temperature β_θ . From this figure, three periods can be distinguished related to the characteristics of the unsteady growth of the CBL. After sunrise, the convective boundary layer starts to develop overlaid by the stable nocturnal boundary layer. At the top of it, the strong capping inversion is preventing thermals to develop. As a result, the boundary layer growth is slow but increasing as the CBL deepens. At around 10:00 LST, the boundary layer top reaches the maximum extension of the previous nocturnal boundary layer. Due to the increase of the capping inversion at this interfacial layer (between the residual of the previous nocturnal boundary layer and the previous day convective boundary layer) the growth is slow down. Then the boundary layer continues to develop but now overlaid by the residual layer of the previous day CBL. The temperature jump at the top of the CBL is lower than previously (see also Fig. 1) and the growth is enhanced due to small temperature gradients across the entrainment zone. The boundary layer doubles its vertical extension within a few hours. At around 12:30 LST, the top of the CBL reaches the free troposphere. The strong capping inversion limits its development, the entrainment velocity dramatically collapse and the CBL depth

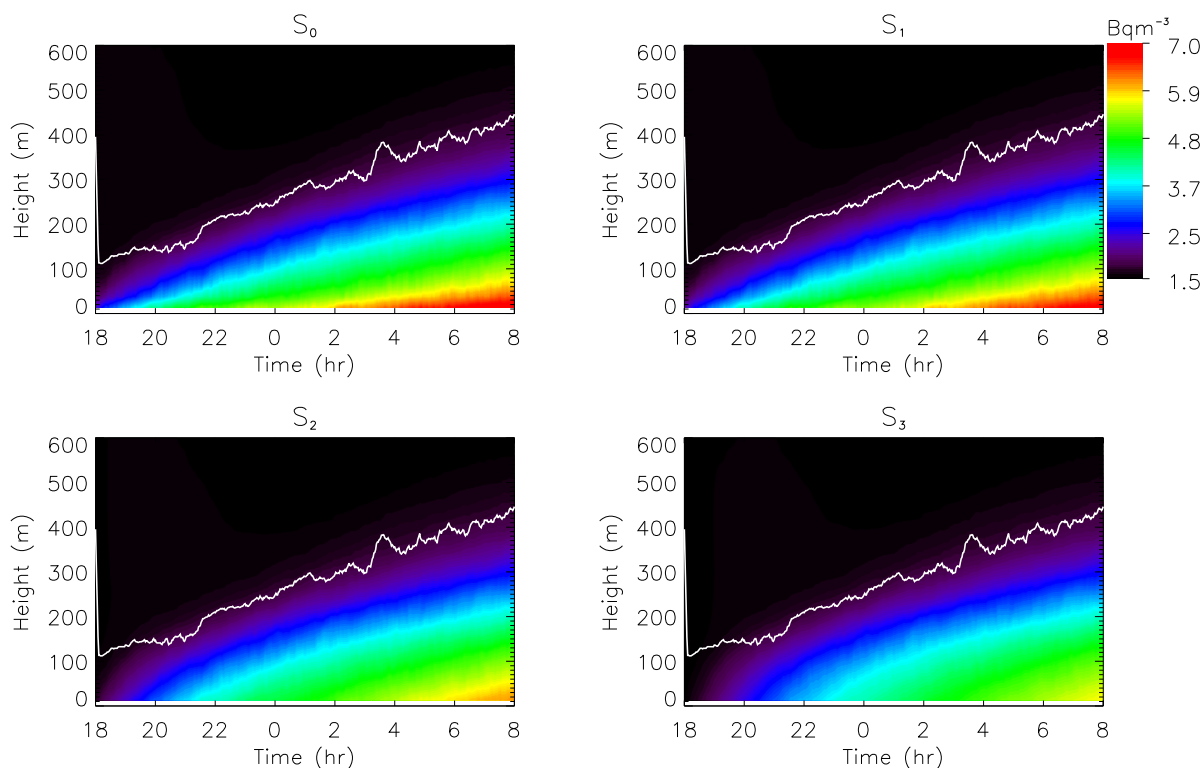


Fig. 7. Time-height plots of the radon and its short-lived daughter concentrations. The boundary layer depth is shown using a solid line. It is defined as the height where the turbulent heat flux is 5% of its surface value (Estournel and Guedalia, 1985).

is evolving toward a steady-state. The sharpness of the peak of entrainment velocity located at around 12:30 LST reflects the strength of the inversion.

Actually these periods are much more distinguishable while focusing on the mixed-layer concentrations of ^{222}Rn and its progeny i.e. $\langle S_i \rangle$ and the ratio of entrainment to the surface flux of ^{222}Rn $\beta_0 = \frac{-(ws_0)_e}{(ws_0)_s}$ where $(ws_0)_e$ and $(ws_0)_s$ are the entrainment and surface flux of S_0 , respectively. The $\langle S_i \rangle$ and β_0 are shown in Fig. 14

- To 09:30 LST: Initialization of convection, a sharp mixed-layer starts to develop overlaid by a strong stratification.
- From 09:30 to 11:00 LST: The mixed-layer is developing within the leftover of the stable nocturnal boundary layer. $\langle S_i \rangle$ decrease due to the entrainment of less radon-concentrated air masses at the top of the CBL. This decrease is limited since air masses above the mixed layer contains S_i that has been trapped during the night.
- From 11:00 to 12:30 LST: The mixed-layer is developing overlaid by the residual layer and $\langle S_i \rangle$ collapse. During the night, the reservoir layer has been almost decoupled from the surface due to the stable stratification

of the nocturnal boundary layer. Since no fresh radon reached this layer, the radon short-lived daughter mixture aged and the system evolved toward secular equilibrium. S_i is less abundant in the reservoir layer than in the leftover of nocturnal boundary layer. Therefore, ventilation is entraining cleaner radon air masses than during the previous period and the decrease of $\langle S_i \rangle$ is more important.

- From 12:30 LST: The mixed-layer top has reached the free troposphere. The ventilation process still occurs but it is less important due to the collapse of w_e and the low concentration gradient at the entrainment interface. The retrieval of the mixed-layer secular equilibrium is facilitated by the entrainment of radon and daughters mixture already in equilibrium.

When the CBL top reaches the free troposphere, large β_0 values persist despite the decline in the entrainment velocity. These large values are due to the large gradient encountered in that region. When β_0 values are large, we found appreciable S_0 gradients within the mixed layer itself, due to the CBL turnover mixing process. This is clearly shown by the 12:00 LST's the profile of radon in Fig. 5. The same feature is also shown in Fig. 4 whenever β_0 is large in magnitude. These features of radon behavior in the CBL indicate a strong

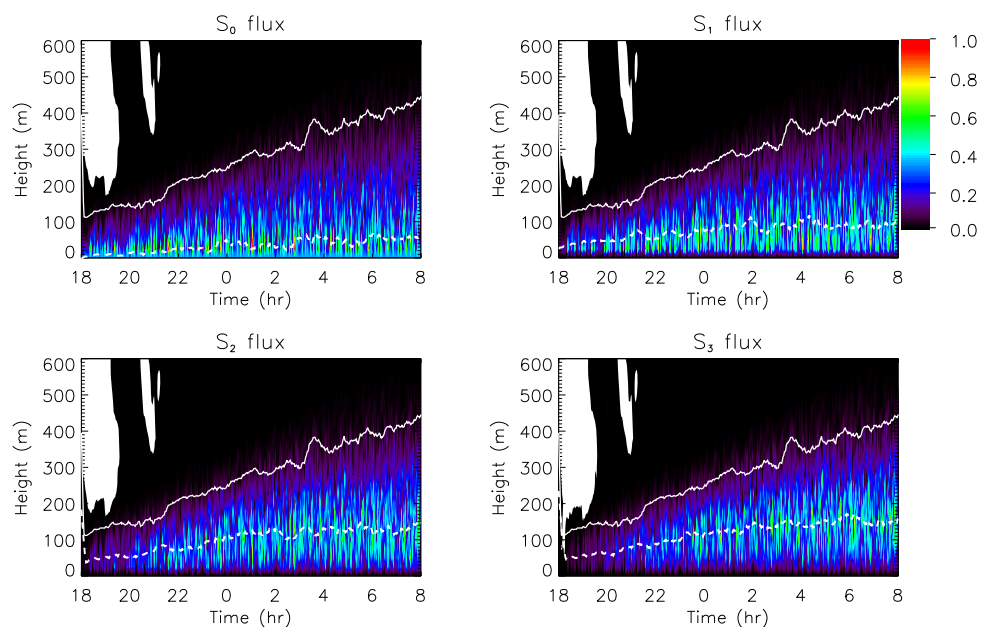


Fig. 8. Time-height plots of the radon and its short-lived daughter dimensionless fluxes. The fluxes have been made dimensionless using their maximum values. The boundary layer depth is shown using a solid line. It is defined as the height where the turbulent heat flux is 5% of its surface value (Estournel and Guedalia, 1985). The areas in white represents downward fluxes. The localisation of the maximum fluxes is shown in dashed lines.

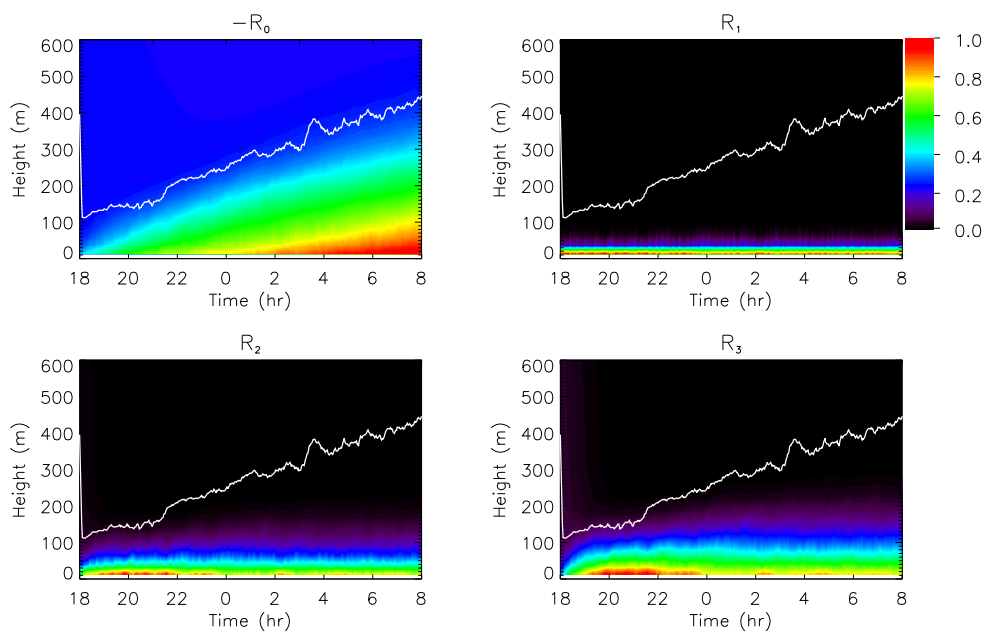


Fig. 9. Time-height plots of the radioactive decay contributions R_i . The contributions have been made dimensionless using their maximum values. The boundary layer depth is shown using a solid line. It is defined as the height where the turbulent heat flux is 5% of its surface value (Estournel and Guedalia, 1985).

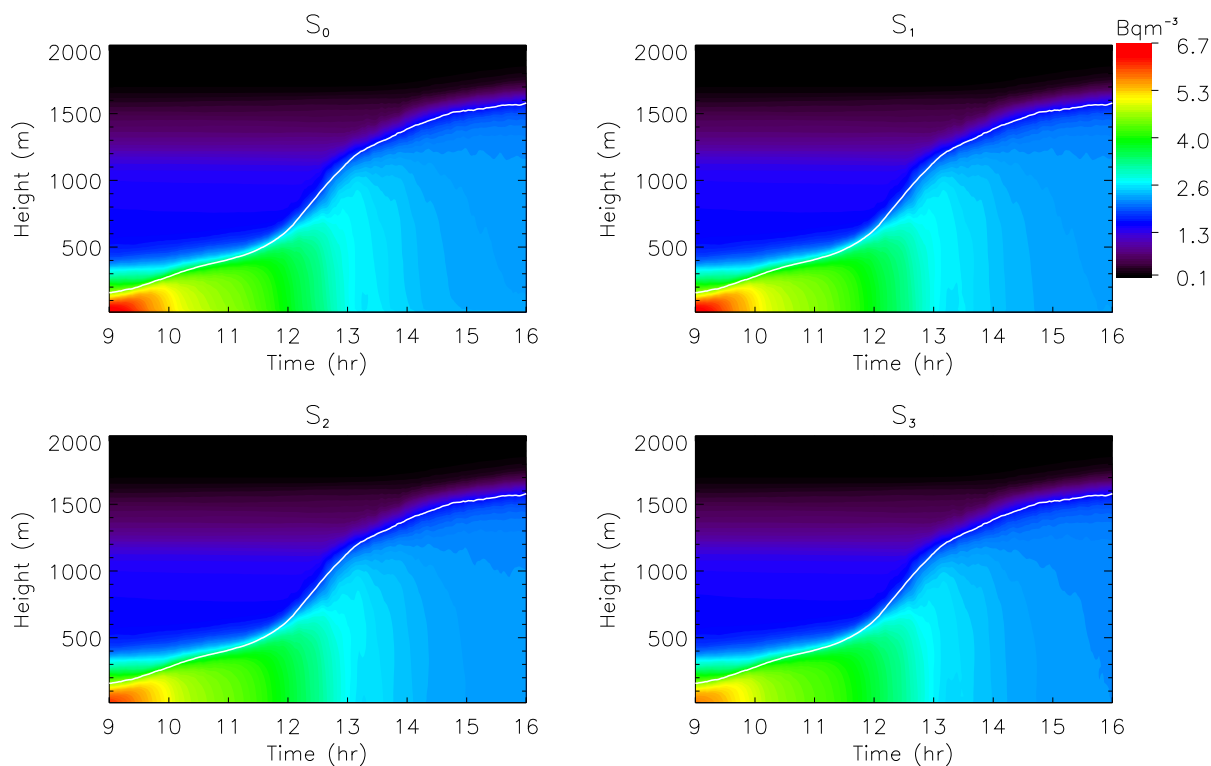


Fig. 10. Time-height plots of the radon and its short-lived daughter concentrations. The daytime boundary layer depth, defined as the altitude where the sensible heat flux is minimum, is also shown using solid white lines.

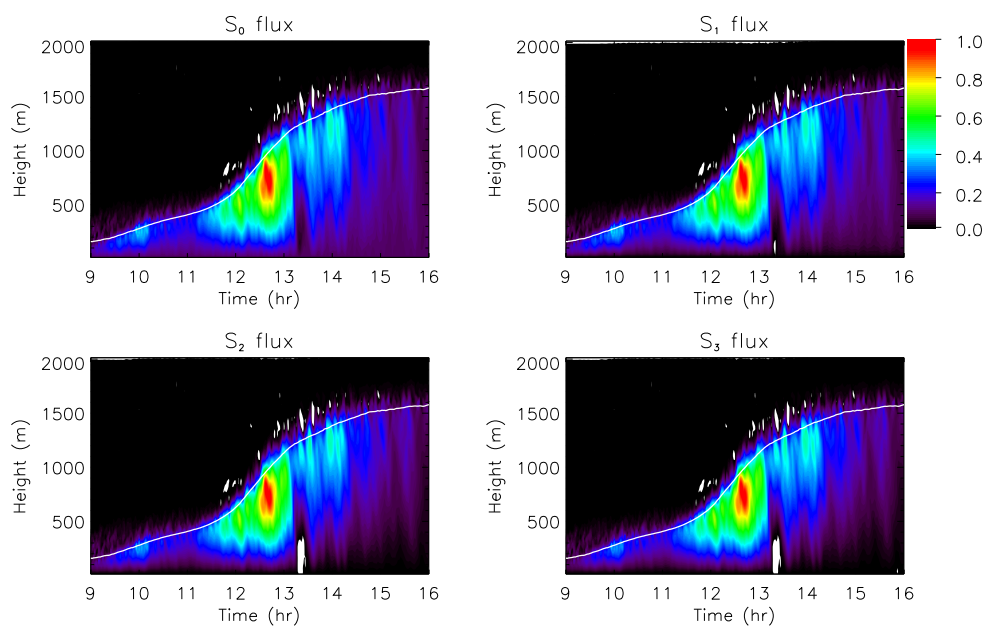


Fig. 11. Time-height plots of the radon and its short-lived daughter dimensionless fluxes. The fluxes have been made dimensionless using their maximum values. The daytime boundary layer depth, defined as the altitude where the sensible heat flux is minimum, is also shown using a solid line.

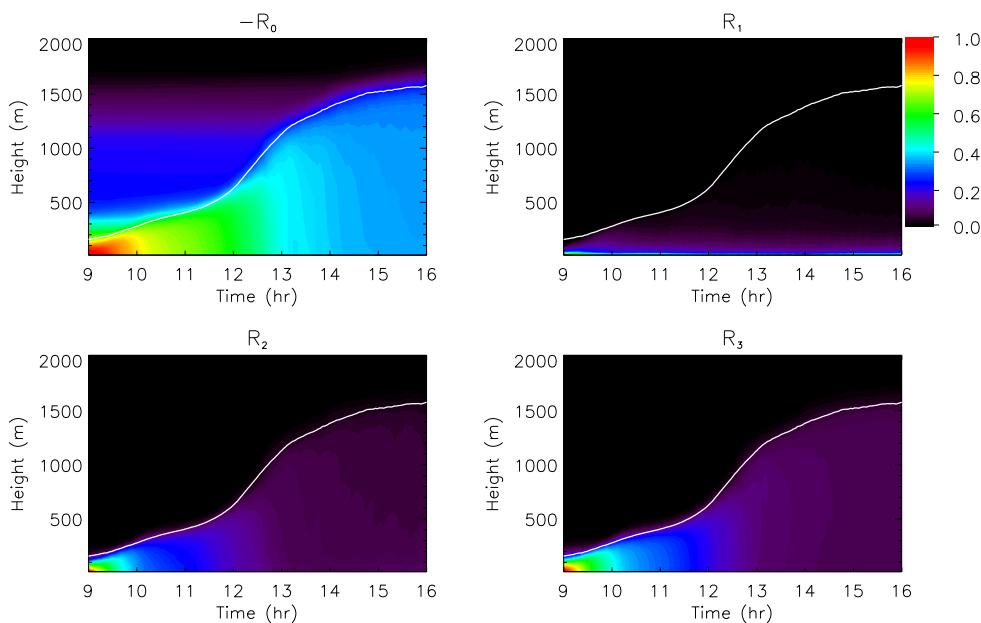


Fig. 12. Time-height plots of the radioactive decay $-R_0$, R_1 , R_2 and R_3 . The contributions have been made dimensionless using their maximum values. The daytime boundary layer depth, defined as the altitude where the sensible heat flux is minimum, is also shown using solid white lines.

potential for the use of radon measurements as a delineator of CBL entrainment.

8 Secular equilibrium

If the radon daughters were subject only to the laws of radioactive decay, the secular equilibrium imposed in the initial activity profiles would be conserved along the simulation. However, departures from the equilibrium can be noticed in Fig. 15 that shows the radon and its short-lived daughters activity ratios. This disequilibrium is more important under stable stratification in the nocturnal boundary layer. Under convective conditions, the ratios evolve toward the equilibrium value of 1.0 that is retrieved after the morning transition. At the end of the day, the surface cooling results in a temperature stable stratification and in the formation of a thin boundary layer isolating the surface from the upper atmosphere layer. In this stable layer, turbulence decays and departures from the equilibrium occur. It is interesting to notice that the equilibrium reached in the mixed layer of the previous day is preserved in the reservoir layer.

There has been extensive measurements of the disequilibrium ratios in the surface layer for various type of stabilities (e.g., Beck and Gogolak, 1979; Hosler and Lockhart, 1965; Hosler, 1966). The largest departures from the secular equilibrium were reported under stable conditions. The disequilibrium ratio was found to be also dependent on both the distance from the surface and the duration of the stabil-

ity regime. Quite a number of one-dimensional models have been formulated to relate the vertical distribution of the radionuclide to the eddy diffusivity and to the exhalation rate of radon (e.g., Jacobi and Andre, 1963; Staley, 1966) and reached the same conclusions.

Several studies in the past have tried to correlate the stability regime with S_0 or the disequilibrium activity ratio. However, even if at first glance it appears that the equilibrium levels might be correlated directly with stability regime in the surface layer, the results shown in Fig. 16 reveal that other boundary layer characteristics are also influential. A given air parcel can be considered as a mixture of radon and its short-lived daughters. At sunset, if this parcel is close to the emission source of radon, it is composed of more freshly emitted radon than “old” radon. Because of the slow decay of radon, this air parcel contains more radon than its short-lived daughters. As a result, radon and its short-lived daughters activity ratios are lower than 1. Throughout the night, the proportion of aging radon trapped in the stable boundary layer tends to increase (compared to “fresh” radon) and the mixture is evolving toward equilibrium. However, since the radioactive half-life of ^{222}Rn is 3.8 days, the night is obviously not long enough to enable the secular equilibrium to be fully established. In Fig. 16, one can notice that the activity ratios collapse in the evening and increase during the night.

During the convective daytime period, turbulent eddy motions are mixing the radon being exhaled from the soil into

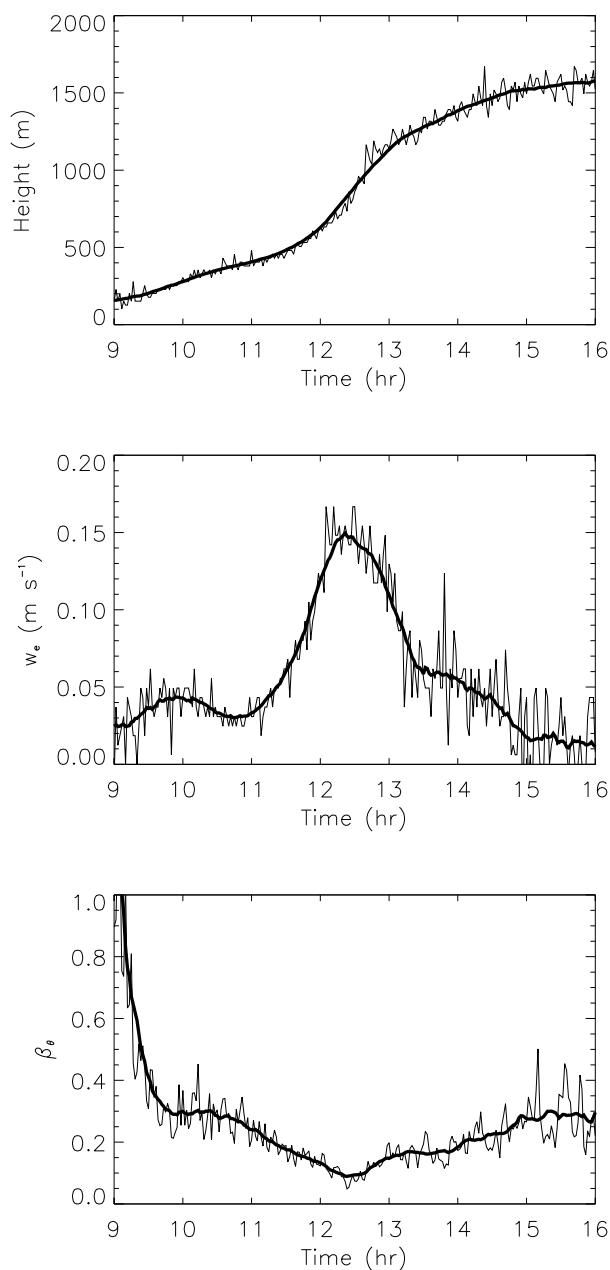


Fig. 13. Boundary layer depth z_i , entrainment velocity w_e and β_θ time evolutions. Smoothed results are also shown in thick solid lines.

aged radon mixture. Due to the mixing and the short turnover time, any air parcel of the CBL contains the same amount of “fresh” radon and “old” radon. Turbulent transport enables the radioactive system to evolve toward the equilibrium. As a result, after the morning transition the equilibrium is reached and the homogeneous composition of the radon and short-lived daughter mixture is maintained by the turnover of the CBL. Figure 16 shows important increases of the activity ra-

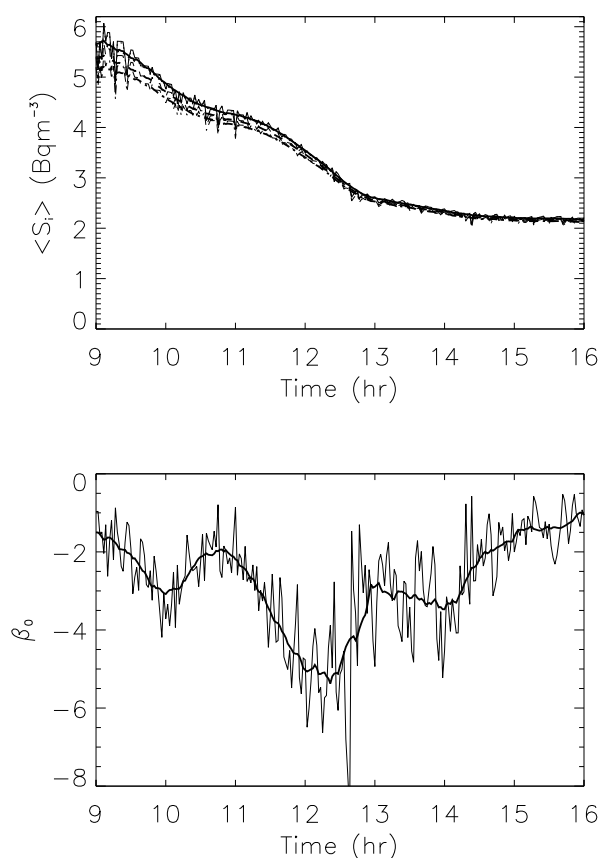


Fig. 14. Mixed layer concentrations $\langle S_i \rangle$ and β_0 time evolution. S_0 , S_1 , S_2 , and S_3 are represented in solid, dotted, dashed and dot-dashed lines, respectively. Smoothed results are also shown in thick lines.

tio during the morning transition. Most of all, our results shows that the activity ratio between radon and its progeny cannot be used solely as an indicator of atmospheric stability for diurnal evolving ABL. As one can clearly see in Fig. 16 two values of the ratio correspond to the same stability value. In this figure, one can notice important differences in the departure from secular equilibrium at dusk between the ratios for different daughters. During the initiation of the stable nocturnal boundary layer, the change of S_1/S_0 activity ratio is rather small while the one of S_3/S_0 can reach 4%. It is of interest to consider whether the driving process of these differences is mixing by nocturnal turbulence or aging of the radionuclide mixture. An appropriate number to investigate the effect of turbulence on the radionuclides is the Damköhler number (Vinuesa and Galmarini, 2007), Da_t defined as the ratio between the integral time-scale of turbulent (τ_t) and the chemical time-scale (τ_c). In Fig. 17, the Damköhler numbers Da_t for Radon and its short-lived daughters are plotted against Obukhov length. Here, we use $\tau_t = z_i/w_*$ for the convective boundary layer and $\tau_t = h/u_*$ for the nocturnal one. z_i

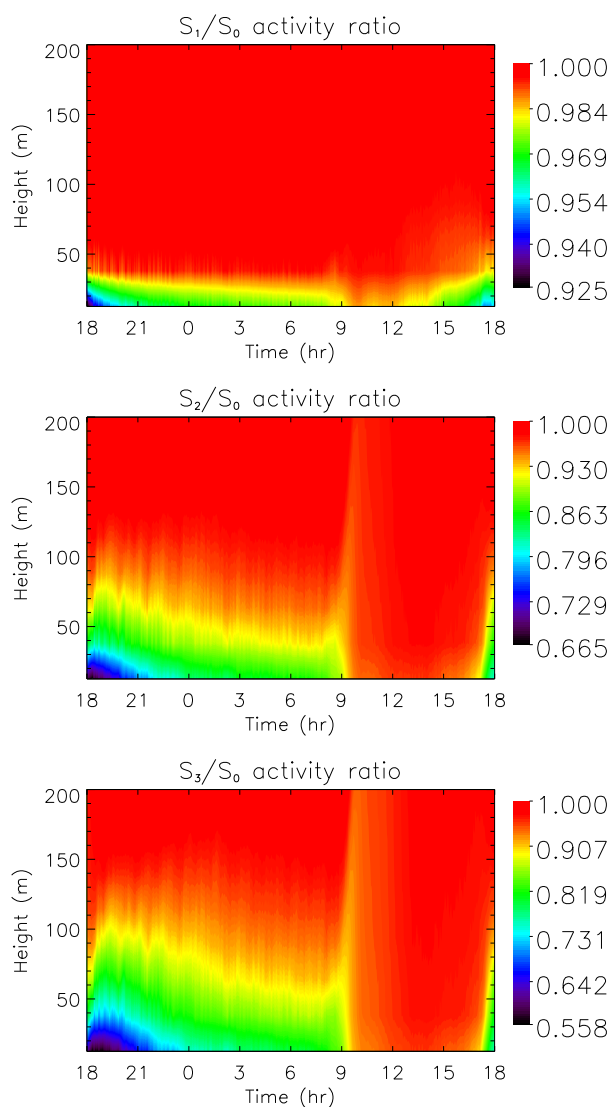


Fig. 15. Radon and its short-lived daughters activity ratio versus time-height.

and h are defined as the altitude where the sensible heat flux is minimum and where the turbulent heat flux is 5% of its surface value (Estournel and Guedalia, 1985), respectively. For the radionuclides, $\tau_c = \lambda_j^{-1}$ with $j=0, 1, 2, 3$ meaning that the Damköhler numbers differ by the radioactive decaying rates. Therefore S_1 and S_2 are the daughters most and least (respectively) affected by turbulence in Fig. 17. However, the most important departure for secular equilibrium is found for S_3 in Fig. 16. This figure clearly shows that nocturnal turbulence does not have the dominant impact on the departure from secular equilibrium at dusk and, as mentioned previously, the driving process is the aging of the mixture of radon and short-lived daughters.

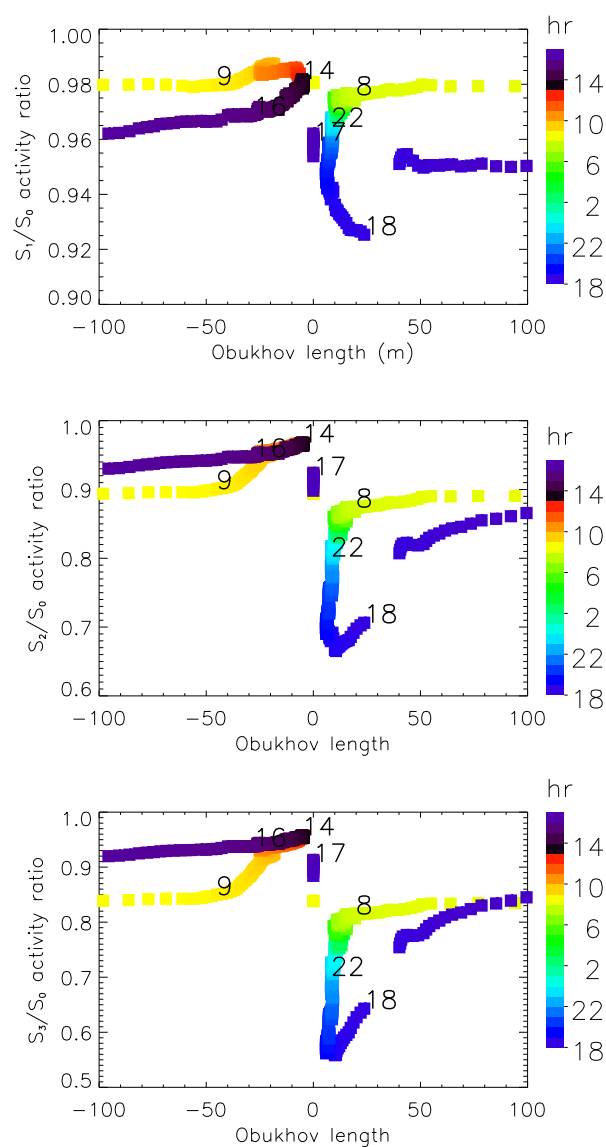


Fig. 16. Radon and its short-lived daughters activity ratio versus Obukhov length at a height of 12.5 m above ground.

9 Conclusions

Numerical experiments were carried out using the state-of-the-art large-eddy simulation together with a new-generation subgrid-scale model to study the diurnal evolution of ^{222}Rn and its progeny in the atmospheric boundary layer. An observed diurnal cycle was successfully simulated and for the first time, the simulation included first-order decaying system represented by the decaying chain of the ^{222}Rn family. By focusing our analysis on the night 33–34 and day 34 of the Wangara experiment, e.g. using the simulation of day 33 as a pre-run, and initializing the ^{222}Rn and short-lived daughters' concentrations as in a secular equilibrium,

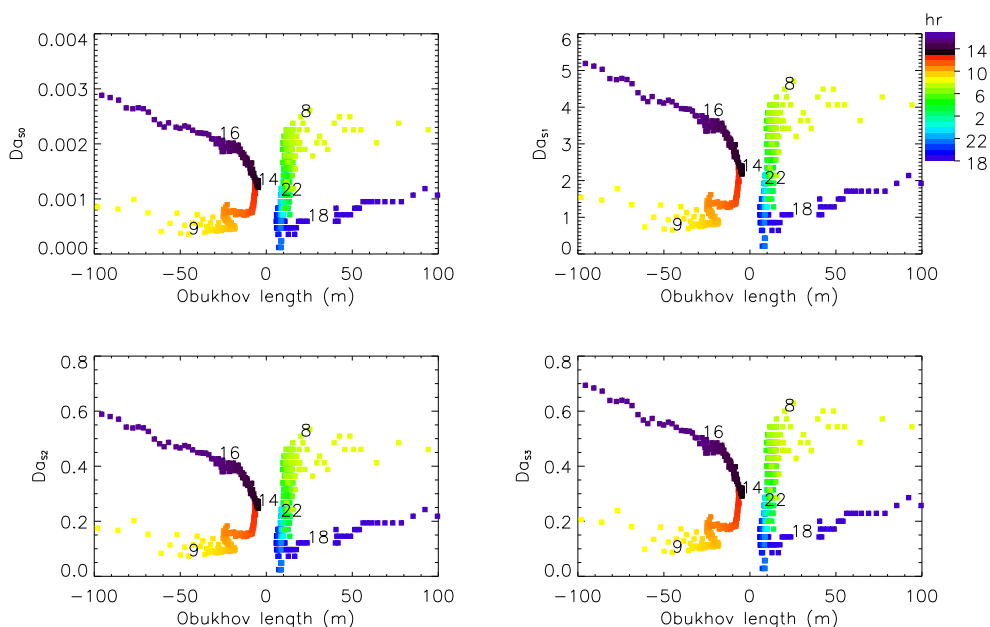


Fig. 17. Radon and its short-lived daughters Damköhler numbers versus Obukhov length.

we were able to reproduce the realistic diurnal evolution of the ^{222}Rn decaying family.

Near the surface, radon concentrations increase during the nocturnal stable period, reaching a maximum near sunrise. Following the breakup of a nocturnal surface-based radiation-type inversion, radon concentrations decrease rapidly, reaching a minimum during the afternoon convective period.

A departure from secular equilibrium between radon and its short-lived daughter products prevails in the stable nocturnal boundary layer. This disequilibrium is attributed to the proximity of the radon source and the weak vertical transport. Since a significant fraction of the radon is fresh, the radon and progeny mixture is deficient in daughters. The mixing induced by convective turbulence induces a fast restoration of the secular equilibrium during the morning transition.

Both turbulent transport and transport asymmetry of the ^{222}Rn daily evolution are important consequence of the entrainment of “clean” air from the reservoir layers above into the boundary layer during its unsteady morning growth period. These entrainment events are responsible for the collapse of the mixed layer concentrations. Our analysis reveals that the spatial and temporal evolution of the concentrations of radon and its daughters is directly related to radioactive decay contribution in which turbulent mixing plays the major role. Thus, turbulent transport affect the dispersion of ^{222}Rn and its progeny by acting preferentially on the radioactive decay.

Acknowledgements. Computational resources were kindly provided by the High Performance Computing Center at the Texas Tech University.

Edited by: M. Ammann

References

- Albertson, J. D. and Parlange, M. B.: Natural integration of scalar fluxes from complex terrain, *Adv. Wat. Res.*, 23, 239–252, 1999.
- Anderson, W., Basu, S., and Letchford, C.: Comparison of dynamic subgrid-scale models for simulations of neutrally buoyant shear-driven atmospheric boundary layer flows, *Env. Fluid Mech.*, 7, 195–215, 2007.
- Andr n, A., Brown, A. R., Graf, J., Mason, P. J., Moeng, C.-H., Nieuwstadt, F. T. M., and Schumann, U.: Large-eddy simulation of a neutrally stratified boundary layer: A comparison of four computer codes, *Q. J. Roy. Meteor. Soc.*, 120, 1457–1484, 1994.
- Andr n, A.: The structure of stably stratified atmospheric boundary layers: a large-eddy simulation study, *Q. J. Roy. Meteor. Soc.*, 121, 961–985, 1995.
- Basu, S. and Port -Agel, F.: Large-eddy simulation of stably stratified atmospheric boundary layer turbulence: a scale-dependent dynamic modeling approach, *J. Atmos. Sci.*, 63, 2074–2091, 2006.
- Basu, S., Port -Agel, F., Foufoula-Georgiou, E., Vinuesa, J.-F., and Pahlow, M.: Revisiting the local scaling hypothesis in stably stratified atmospheric boundary-layer turbulence: an integration of field and laboratory measurements with large-eddy simulations, *Boundary-Layer Meteorol.*, 119, 473–500, 2006.
- Basu, S., Vinuesa, J.-F., and Swift, A.: Dynamic LES modeling of a diurnal cycle, *J. Appl. Meteorol. Clim.*, in press, 2007.
- Beare, R. J., Macvean, M. K., Holtslag, A. A. M., Cuxart, J., Esau, I., Golaz, J.-C., Jimenez, M. A., Khairoutdinov, M., Kosovic, B., Lewellen, D., Lund, T. S., Lundquist, J. K., McCabe, A., Moene, A. F., Noh, Y., Raasch, S., and Sullivan, P.: An intercom-

- parison of large-eddy simulations of the stable boundary layer, *Boundary-Layer Meteorol.*, 118, 247–272, 2006.
- Beck, H. L. and Gogolak, C. V.: Time dependent calculation of the vertical distribution of ^{222}Rn and its decay products in the atmosphere, *J. Geophys. Res.*, 84, 3139–3148, 1979.
- Bou-Zeid, E., Meneveau, C., and Parlange, M.: A scale-dependent Lagrangian dynamic model for large eddy simulation of complex turbulent flows, *Phys. Fluids*, 17, 025105, doi:10.1063/1.1839152, 2005.
- Brown, A. R., Derbyshire, S. H., and Mason, P. J.: Large-eddy simulation of stable atmospheric boundary layers with a revised stochastic subgrid model, *Q. J. Roy. Meteor. Soc.*, 120, 1485–1512, 1994.
- Chow, F. K., Street, R. L., Xue, M., and Ferziger, J. H.: Explicit filtering and reconstruction turbulence modeling for large-eddy simulation of neutral boundary layer flow, *J. Atmos. Sci.*, 62, 2058–2077, 2005.
- Clarke, R. H., Dyer, A. J., Brook, R. R., Reid, D. G., and Troup, A. J.: The Wangara experiment: boundary layer data, Paper No. 19, Div. Meteorol. Physics Aspendale, CSIRO, Australia, 362 pp., 1971.
- Deardorff, J. W.: Preliminary results from numerical integrations of the unstable planetary boundary layer, *J. Atmos. Sci.*, 27, 1209–1211, 1970.
- Deardorff, J. W.: Numerical investigation of neutral and unstable planetary boundary layers, *J. Atmos. Sci.*, 29, 91–115, 1972.
- Deardorff, J. W.: Three-dimensional numerical study of the height and mean structure of a heated planetary boundary layer, *Boundary-Layer Meteorol.*, 7, 81–106, 1974a.
- Deardorff, J. W.: Three-dimensional numerical study of turbulence in an entraining mixed layer, *Boundary-Layer Meteorol.*, 7, 199–226, 1974b.
- Deardorff, J. W.: Stratocumulus-capped mixed layers derived from a three-dimensional model, *Boundary-Layer Meteorol.*, 18, 495–527, 1980.
- Dentener, F., Feichter, J., and Jeuken, A.: Simulation of the transport of Rn-222 using on-line and off-line global models at different horizontal resolutions: a detailed comparison with measurements, *Tellus*, 51B, 573–602, 1999.
- Esau, I.: Simulation of Ekman boundary layers by large eddy model with dynamic mixed subfilter closure, *Environ. Fluid Mech.*, 4, 273–303, 2004.
- Estournel, C. and Guedalia, D.: Influence of geostrophic wind on atmospheric nocturnal cooling, *J. Atmos. Sci.*, 42, 2695–2698, 1985.
- Galmarini, S.: One year of ^{222}Rn concentration in the atmospheric surface layer, *Atmos. Chem. Phys.*, 6, 2865–2887, 2006.
- Genthon, C. and Armengaud, A.: Radon-222 as a comparative tracer of transport and mixing in 2 general-circulation models of the atmosphere, *J. Geophys. Res.*, 100, 2849–2866, 1995.
- Hess, G. D., Hicks, B. B., and Yamada, T.: The impact of the Wangara experiment, *Boundary-Layer Meteorol.*, 20, 135–174, 1981.
- Hicks, B. B.: An analysis of Wangara micrometeorology: surface stress, sensible heat, evaporation, and dewfall. Air Resources Laboratories, Silver Spring, Maryland, Tech. Rep. NOAA Technical Memorandum ERL ARL-104, 36 pp., 1981.
- Hosler, C. R. and Lockhart, L. B.: Simultaneous measurement of ^{222}Rn , ^{214}Pb and ^{214}Bi in air near the ground, *J. Geophys. Res.*, 70, 4537–4546, 1965.
- Hosler, C. R.: Meteorological effects on atmospheric concentrations of Radon (Rn^{222}), RaB (Pb^{214}), and RaC (Bi^{214}) near the ground, *Mon. Weather Rev.*, 94, 89–99, 1966.
- Jacob, D. J., Prather, M. J., Rasch, P. J., Shia, R. L., Balkanski, Y. J., Beagley, S. R., Bergmann, D. J., Blackshear, W. T., Brown, M., Chiba, M., Chipperfield, M. P., deGrandpre, J., Dignon, J. E., Feichter, J., Genthon, C., Grose, W. L., Kasibhatla, P. S., Kohler, I., Kritz, M. A., Law, K., Penner, J. E., Ramonet, M., Reeves, C. E., Rotman, D. A., Stockwell, D. Z., VanVelthoven, P. F. J., Verver, G., Wild, O., Yang, H., and Zimmermann, P.: Evaluation and intercomparison of global atmospheric transport models using Rn-222 and other short-lived tracers, *J. Geophys. Res.*, 102, 5953–5970, 1997.
- Jacobi, W. and Andre, K.: The vertical distribution of ^{222}Rn , ^{220}Rn and their decay products in the atmosphere, *J. Geophys. Res.*, 68, 3799–3814, 1963.
- Khanna, S. and Brasseur, J. G.: Analysis of Monin-Obukhov similarity from large-eddy simulation, *J. Fluid Mech.*, 345, 251–286, 1997.
- Kumar, V., Kleissl, J., Meneveau, C., and Parlange, M. B.: Large-eddy simulation of a diurnal cycle of the atmospheric boundary layer: Atmospheric stability and scaling issues, *Water Resour. Res.*, 42, W06D09, doi:10.1029/2005WR004651, 2006.
- Kosović, B.: Subgrid-scale modelling for the large-eddy simulation of high-Reynolds-number boundary layers, *J. Fluid Mech.*, 338, 151–182, 1997.
- Kosović, B. and Curry, J. A.: A large eddy simulation study of a quasi-steady, stably stratified atmospheric boundary layer, *J. Atmos. Sci.*, 57, 1052–1068, 2000.
- Lewellen, D. C. and Lewellen, W. S.: Large-eddy boundary layer entrainment, *J. Atmos. Sci.*, 55, 2645–2665, 1998.
- Li, Y. H. and Chang, J. S.: A three-dimensional global episodic tracer transport model. 1. Evaluation of its processes by radon 222 simulations, *J. Geophys. Res.*, 101, 25 931–25 947, 1996.
- Lin, C.-L., McWilliams, J. C., Moeng, C.-H., and Sullivan, P. P.: Coherent structures and dynamics in a neutrally stratified planetary boundary layer flow, *Phys. Fluids*, 8, 2626–2639, 1996.
- Mason, P. J. and Thomson, D. J.: Large-eddy simulations of the neutral-static-stability planetary boundary layer, *Q. J. Roy. Meteor. Soc.*, 113, 413–443, 1987.
- Mason, P. J.: Large-eddy Simulation of the Convective Atmospheric Boundary Layer, *J. Atmos. Sci.*, 46, 1492–1516, 1989.
- Mason, P. J. and Derbyshire, S. H.: Large-eddy simulation of the stably-stratified atmospheric boundary layer, *Boundary-Layer Meteorol.*, 53, 117–162, 1990.
- Moeng, C. H. and Wyngaard, J. C.: Statistics of conservative scalars in the convective boundary layer, *J. Atmos. Sci.*, 41, 3161–3169, 1984.
- Moeng, C. H. and Sullivan, P. P.: A comparison of shear- and buoyancy-driven planetary boundary layer flows, *J. Atmos. Sci.*, 51, 999–1022, 1994.
- Nieuwstadt, F. T. M., Mason, P. J., Moeng, C.-H., and Schumann, U.: Large-eddy simulation of the convective boundary layer: a comparison of four computer codes, in: *Turbulent Shear Flows 8*, edited by: Durst, F., Friedrich, R., Launder, B. E., Schmidt, F. W., Schumann, U., and Whitelaw, J. H., Springer, 347–367, 1991.
- Porté-Agel, F., Meneveau, C., and Parlange, M. B.: A scale-dependent dynamic model for large-eddy simulations: applica-

- tion to a neutral atmospheric boundary layer, *J. Fluid Mech.*, 415, 261–284, 2000.
- Porté-Agel, F.: A scale dependent dynamic model for scalar transport in LES of the atmospheric boundary layer, *Bound.-Layer Meteorol.*, 112, 81–105, 2004.
- Saiki, E. M., Moeng, C.-H., and Sullivan, P. P.: Large-eddy simulation of the stably stratified planetary boundary layer, *Boundary-Layer Meteorol.*, 95, 1–30, 2000.
- Schumann, U.: Large-eddy simulation of turbulent diffusion with chemical reactions in the convective boundary layer, *Atmos. Environ.*, 23, 1713–1729, 1989.
- Staley, D. O.: The diurnal oscillations of radon and thoron and their decay products, *J. Geophys. Res.*, 71, 3357–3367, 1966.
- Stoll, R., and Porté-Agel, F.: Dynamic subgrid-scale models for momentum and scalar fluxes in large-eddy simulations of neutrally stratified atmospheric boundary layers over heterogeneous terrain, *Water. Resour. Res.*, 42, W01409, doi:10.1029/2005WR003989, 2006.
- Sullivan, P. P., Moeng, C.-H., Stevens, B., Lenschow, D. H., and Mayor, S. D.: Structure of the entrainment zone capping the convective atmospheric boundary layer, *J. Atmos. Sci.*, 55, 3042–3064, 1998.
- Sykes, R. I. and Henn, D. S.: Large-eddy simulation of turbulent sheared convection, *J. Atmos. Sci.*, 46, 1106–1118, 1989.
- UNSCEAR: Sources and effects of ionizing radiation. Volume 1: sources. United Nations Scientific Committee on Effects of Atomic Radiation, UN publication, New York, 2000.
- Vinuesa, J.-F. and Porté-Agel, F.: A dynamic similarity sub-grid model for chemical transformations in LES of the atmospheric boundary layer, *Geophys. Res. Lett.*, 32, L03814, doi:10.1029/2004GL021349, 2005.
- Vinuesa, J.-F. and Galmarini, S.: Characterization of the ^{222}Rn family turbulent transport in the convective atmospheric boundary layer, *Atmos. Chem. Phys.*, 7, 697–712, 2007, <http://www.atmos-chem-phys.net/7/697/2007/>.
- Yamada, T. and Mellor, G.: A simulation of the Wangara atmospheric boundary layer data, *J. Atmos. Sci.*, 32, 2309–2329, 1975.